Supplementary Information for

Ultrasensitive bionic photonic-electronic skin with wide red-shift mechanochromic response

Tianqi Wang[1,‡], Lei Chen[1,‡], Haogeng Liu[1], Haoran Zhu[1], Zijie Zeng[1], Yixin Lu[1], Ping Zhang[3], Yaofei Chen[1], Yue Huang[4], Gui-Shi Liu[1,*], Yunhan Luo [1,*] and Zhe Chen[2,*]

[1] Guangdong Provincial Key Laboratory of Optical Fiber Sensing and Communications, Key Laboratory of Visible Light Communications of Guangzhou, Key Laboratory of Optoelectronic Information and Sensing Technologies of Guangdong Higher Education Institutes, College of Physics & Optoelectronic Engineering, Jinan University, Guangzhou 510632, China

[2] Jihua Laboratory, Foshan 528200, China

[3] Department of Dermatology, Wuhan No.1 Hospital, Wuhan 430022, China

[4] School of Stomatology, Jinan University, Guangzhou 510632, China

[‡] These authors contributed equally.

* guishiliu@163.com

* yunhanluo@jnu.edu.cn

* thzhechen@jnu.edu.cn

1. Supporting Note S1. Mechanoelectrical response mechanism of the MXene/AgNW-PDMS

The MXene/AgNWs sensing layer can be simplified as the resistance R_M of the MXene layer and the resistance R_A of the AgNW layer in parallel. Its total resistance Furthermore, the upper NP array in the PE-skin is embedded into the PDMS surface with a limit protruding (tens of nanometers in height, see Fig. S18). R is given by:

$$R = \frac{R_M \times R_A}{R_M + R_A} \tag{1}$$

Similar to metal nanomembrane sensors, the resistance R_M of the cracked MXene membrane is related to the strain ε in power law:[1, 2]

$$R_M = R_{M0}\left(1 + \left(\frac{\varepsilon}{\varepsilon_0}\right)^n\right) \tag{2}$$

where ε_0 and n are constant parameters, R_{M0} is the initiate resistance of the MXene membrane.

The underlying AgNWs can maintain conductive pathways due to outstanding strain dissipation and slippage of NW networks in A-PDMS (Figure 5c).[3] The resistance R_A of the AgNW-PDMS can be characterized by the tunneling resistances at the junctions between two NWs:[4]

$$R_A = R_{A0}(1 + \varepsilon)e^{a\varepsilon} \tag{3}$$

$$a = \frac{4\pi}{h} d_0 \sqrt{2 m_e E_B} \tag{4}$$

where R_{A0} is the initial resistance, d_0 is the average tunneling distance between adjacent NWs at rest, h is the Plank's constant, m_e is the electron mass, and E_B is the tunneling potential barrier.

Combining Equation (1), (2), and (4), the $\Delta R/R_0$ is related to the applied strain as follow:

$$\frac{\Delta R}{R_0} = \frac{(R_{M0}/R_{A0}+1)(1+\varepsilon)e^{a\varepsilon}}{R_{M0}/R_{A0}+(1+\varepsilon)e^{a\varepsilon}/(1+b\varepsilon^n)} - 1 \tag{5}$$

where $b = (\varepsilon_0)^{-n}$ is the constant parameter.

2. Supporting Figures

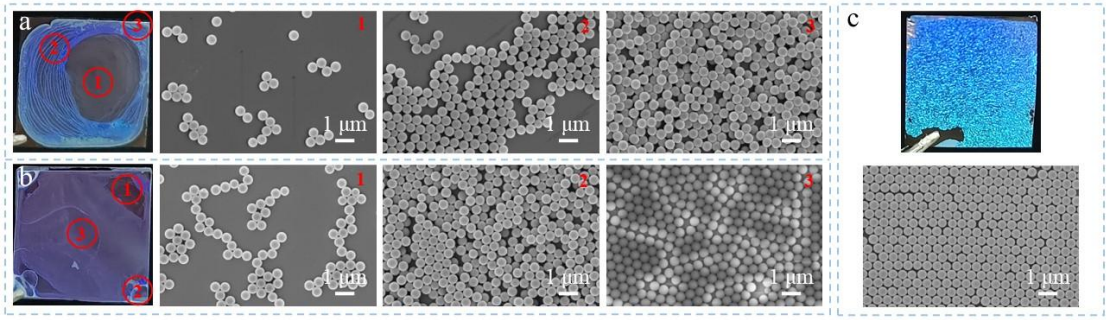

Figure S1. Photographs and SEM images of polystyrene NP arrays on silicon. a) the NP array produced by drop casting of 1wt% NP dispersion. b) the NP array obtained by spin coating of 1wt% NP dispersion. c) Highly ordered NP array fabricated by the Marangoni self-assembly method.

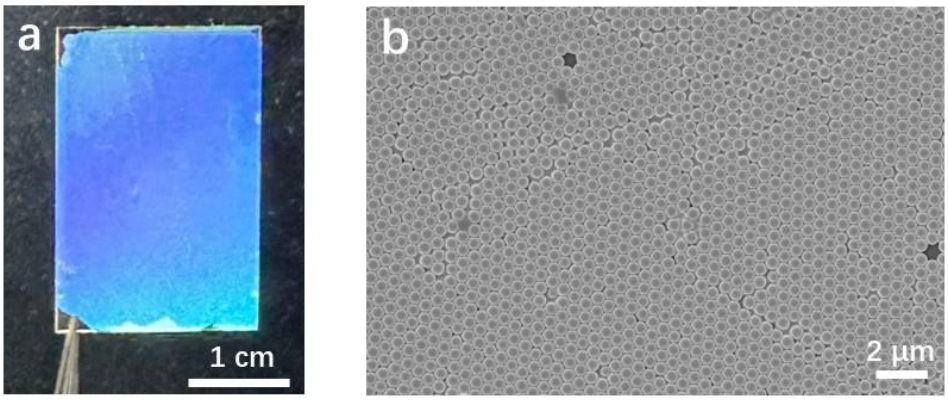

Figure S2. a) Photograph of the NP array transferred from air-water interface to glass, sample size: 2 cm × 3 cm. b) The SEM image of the ordered, close-packed NP array.

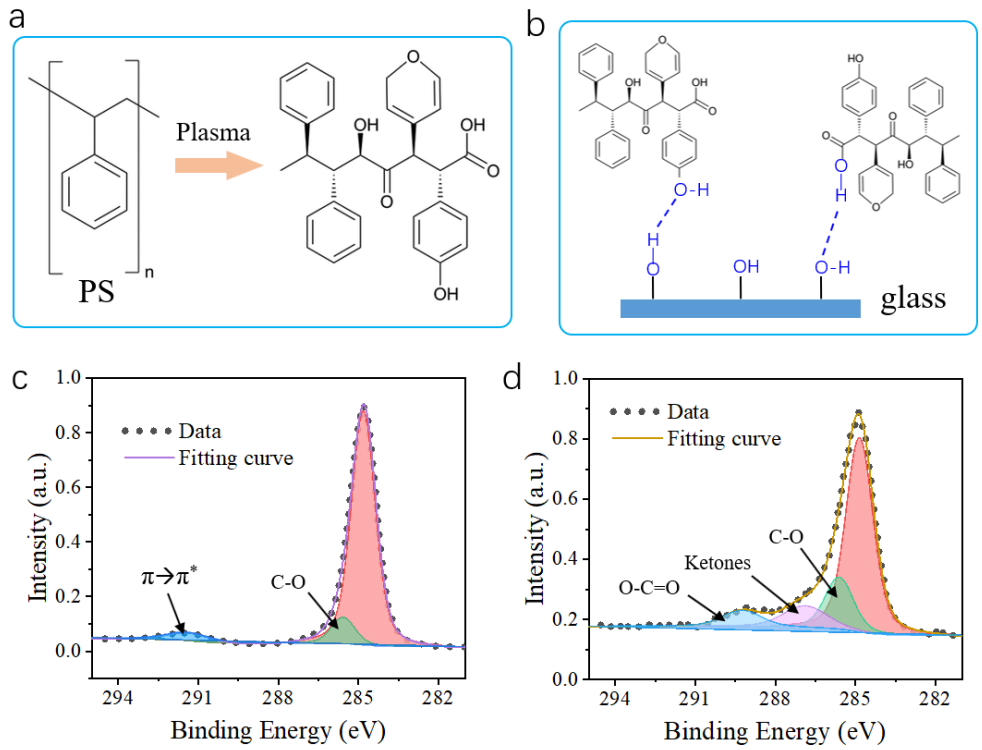

Figure S3. a) Air-plasma-induced modification of polystyrene. b) Schematic of the hydrogen-bonding interaction between oxidized PS and hydroxylated glass. XPS spectra of c) raw polystyrene NPs and d) plasma-treated polystyrene NPs.

The high-resolution spectrum c) of carbon C 1s of raw PS shows three components: C-C at a binding energy of 284.8 eV, C-O at 285.6 eV arising from partial oxidation, and π-π* shake-up peak at 291.5 eV which is characteristic of aromatic rings of the PS macromolecule.[5] After air plasma treatment, the band corresponding to C-O is more notable and two new bands at binding energies of 286.9 eV (ketones) and 289.2 eV (carboxylic acids) are observed. In addition, the characteristic π-π* band of aromatic rings is no longer observable, indicating that the structure of the raw PS is occulted by the new oxidized groups (e.g., O-C=O, ketones, C-O).

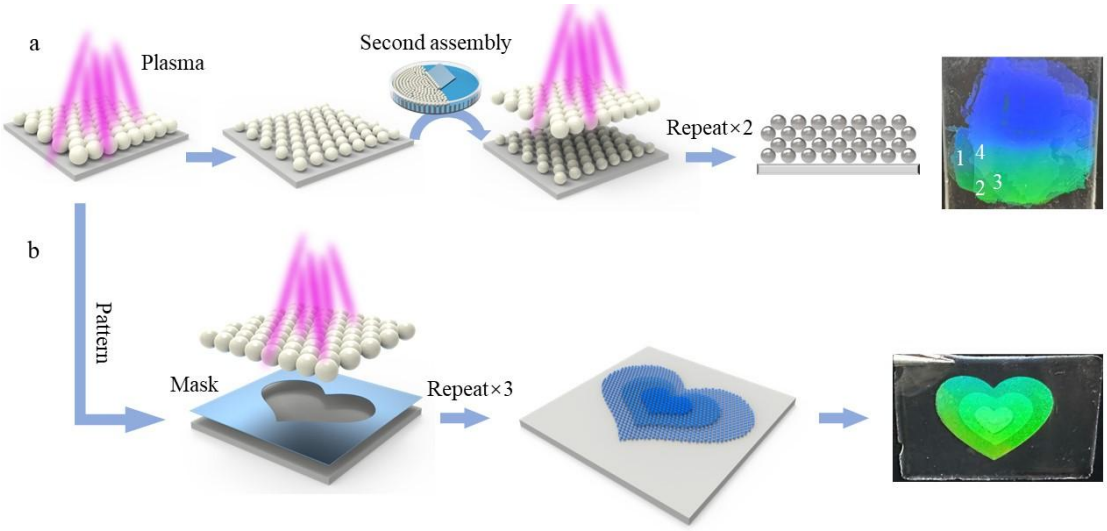

Figure S4. a) Fabrication procedure of the multi-layered PCC film, the right photograph is the 4-layer PCC film. b) Schematic of multi-monolayer patterning of the PCC, the right photograph is the patterned three-monolayer PCC film.

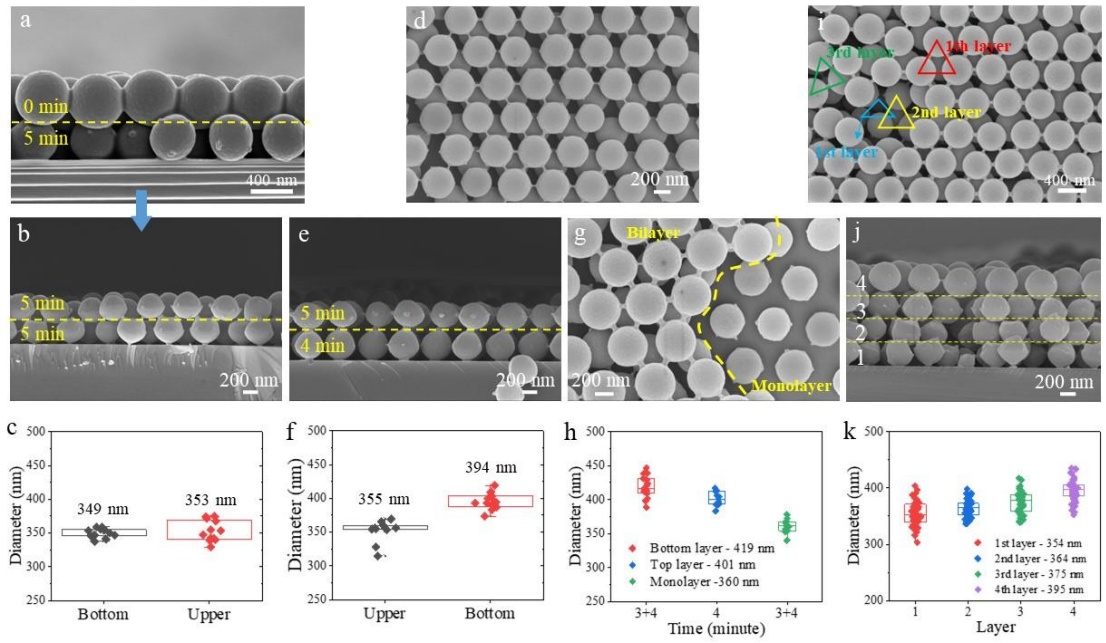

Figure S5. a) SEM image of the bilayered NP array, in which the upper and bottom layers were plasma-treated for 0 and 5 minutes, respectively. b) SEM image of the bilayered NP array with 5-minute plasma treatment for each layer and c) the according statistics of NP diameter. d) Top-view and e) cross-sectional SEM image of the bilayered NP array with 5-minute treatment for the upper layer and 4-minute treatment for the bottom layer and f) the according statistics of NP diameter. g) SEM image of the boundary between a monolayer and a bilayer, where the bottom layer was treated for 3 minutes and the upper layer for 4 minutes, and the monolayer in the right for 3 + 4 minutes, and h) the according statistics of NP diameter. i) Top-view SEM image of four layers of the NP array with a defect, showing four layers. j) Cross-sectional SEM image of four layers of the NP array with 4-minute treatment for each layer, and k) the according statistics of NP diameter of each layer.

From the above SEM images, we can arrive at straight-forward conclusions: (1) the as-transferred upper layer can maintain an ordered, compacted NP array; (2) Each monolayer is distinguishable and stacks one another with well-defined interfaces and ordered structures. Further analysis of NP diameters of the bilayer samples indicates that the average diameters of the bottom layer are 354 nm for 5-minute plasma treatment (b-c) and 394 nm for 4-minute treatment (e-f). The two values are close to the values of a monolayer with the same plasma treatment time (**Figure 2a**). The above results indicate that the top layer well shields the bottom layer from plasma etching, the bottom layer is only slightly etched (4 nm in diameter). The shielding effect can be observed at

the boundary of another sample between a bilayer and a monolayer (e-f). In Figure S5(j-k), each lower layer was etched more by about 14 nm on average. If adopting the etching rate of the 4th layer (105/240=0.44 nm/s), a gradient (30 s) of plasma treatment for four layers (150, 180, 210, 240 s) can produce the same size for each layer. However, the repeatability error of experiments can be as high as 20 nm in NP diameter under the same condition (may be due to non-uniform plasma within the chamber and/or from time to time). Considering the first three layers (354, 364, 375 nm) only have a gradient of about 10 nm and the center-to-center distance between adjacent NPs is the same for all samples (about 500 nm), it is reasonable to use the same plasma treatment time and ignore the small size difference in the trilayer PC herein. The vivid colors with a large color gamut of our PC support the above argument.

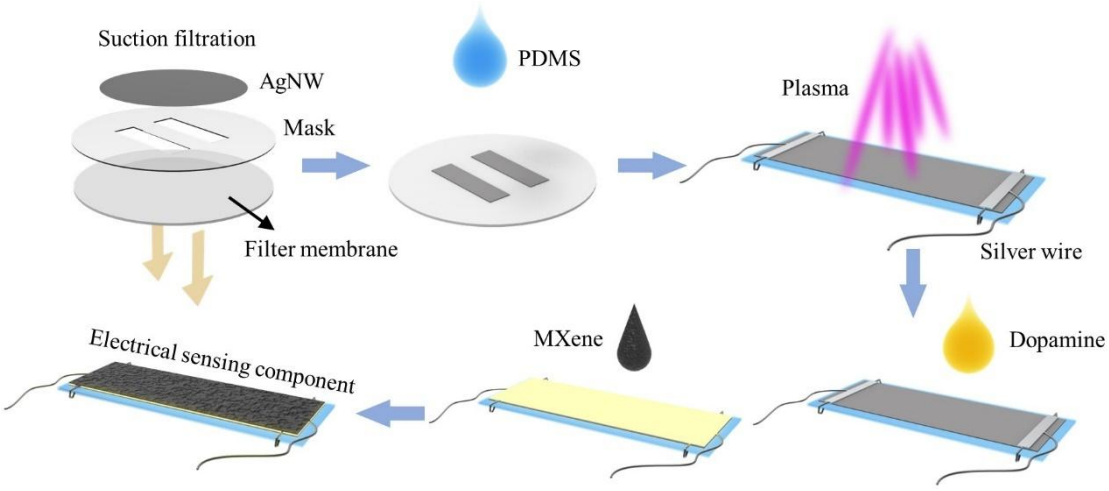

Figure S6. Schematic of the fabrication process of the MXene/AgNW-PDMS component in the PE-skin.

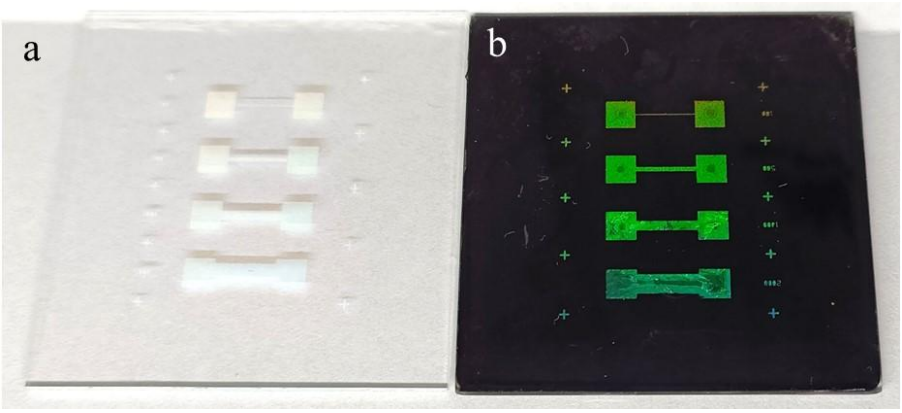

Figure S7. Comparison of the color saturation of the PPC a) without and b) with the underlying MXene membrane.

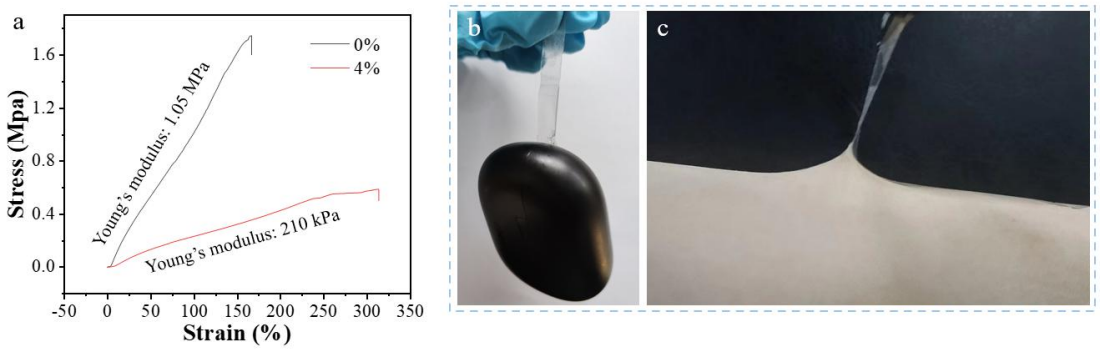

Figure S8. a) Tensile stress-strain curves of the PDMS without and with the surfactant Zonyl FS-300 (4 wt%). b) Photographs of the A-PDMS withstanding 40-g AirPods and c) being peeled from the skin, showing strong adhesion strength. Note that the A-PDMS is coated on a PET polymer to conduct the adhesion tests in the photographs of b) and c).

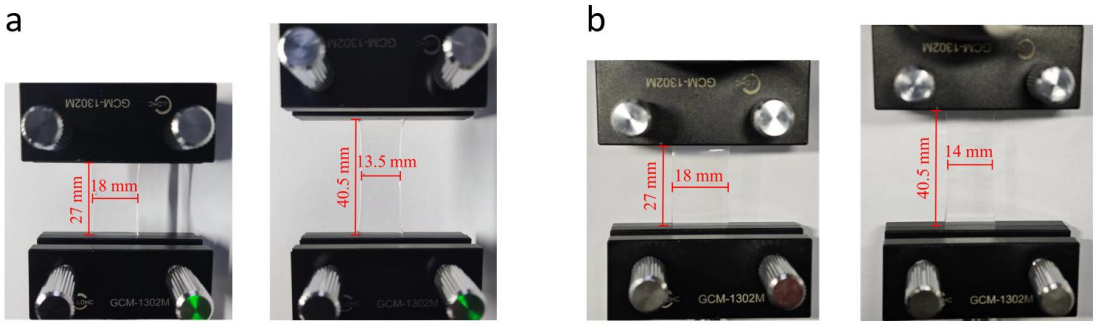

Figure S9. Photographs of a) raw PDMS and b) A-PDMS before and after stretching for the estimation of Poisson ratio. The Poisson's ratios of raw PDMS and A-PDMS are also measured to be 0.5 and 0.44, respectively.

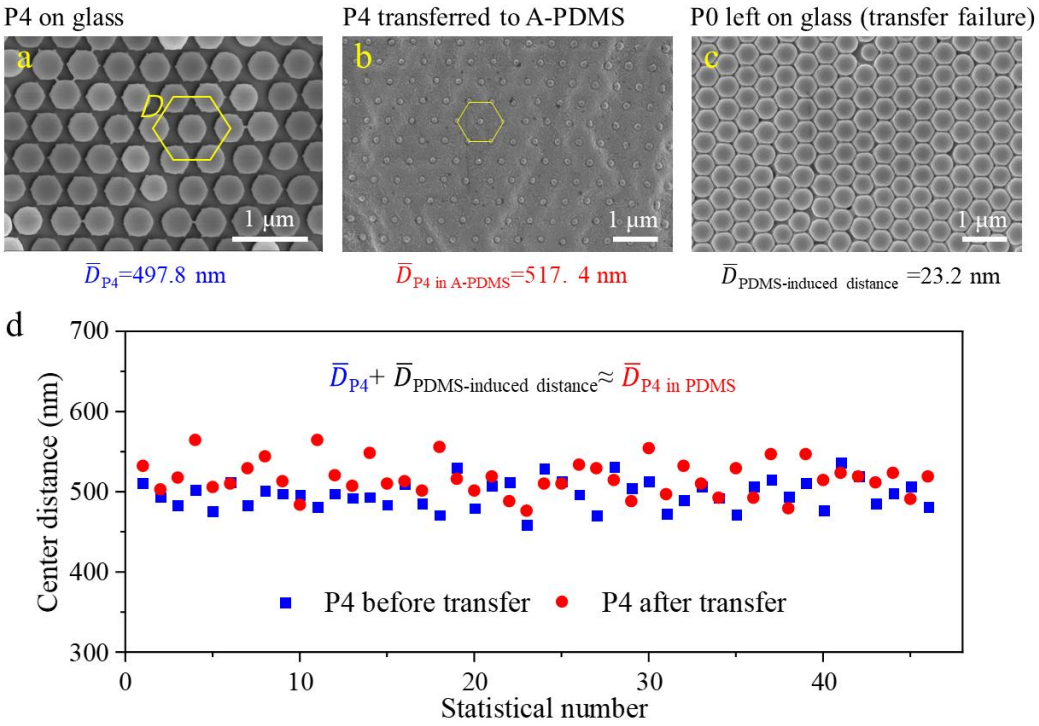

Figure S10. SEM images of a) the PS nanoparticle array after 4-minute plasma etching (P4), b) the P4 array transferred into the PDMS surface, and c) the nanoparticle array (without plasma treatment, P0) which was first cast with PDMS and left on glass after peeling PDMS off (transfer failure). All the NP arrays with and without PDMS casting have highly ordered structures.

The average center distance ($\overline{D}$) of the P4 sample (4-minute plasma treatment) was determined to be 497.8 nm and slightly increased to 517.4 nm after transferring to PDMS. The distance increase (around 20 nm) is about equal to the average interparticle distance (23.2 nm) of the PDMS-casted NP array that is close-packed before the casting (without plasma treatment, P0). Noted that the NP array is left on glass after peeling off PDMS (transfer failure). Therefore, the PDMS casting does not change the order structure but can slightly increase lattice distance by about 20 nm.

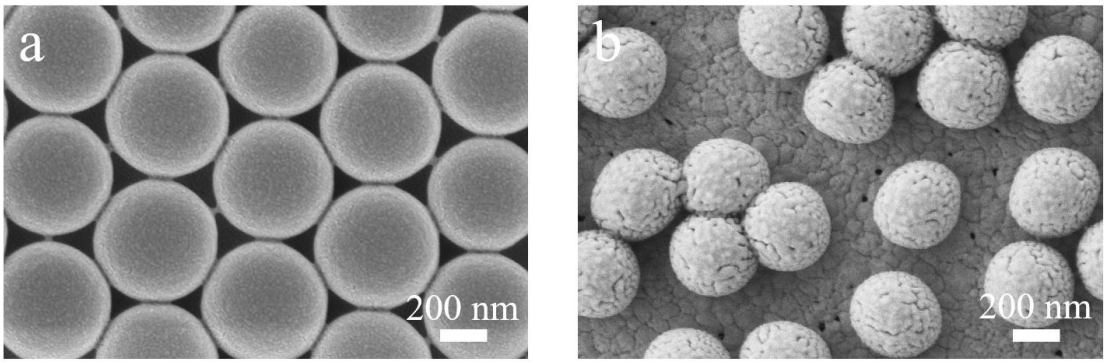

Figure S11. SEM images of a) a raw polystyrene NP array and b) a plasma-treated NP array (6-minute treatment).

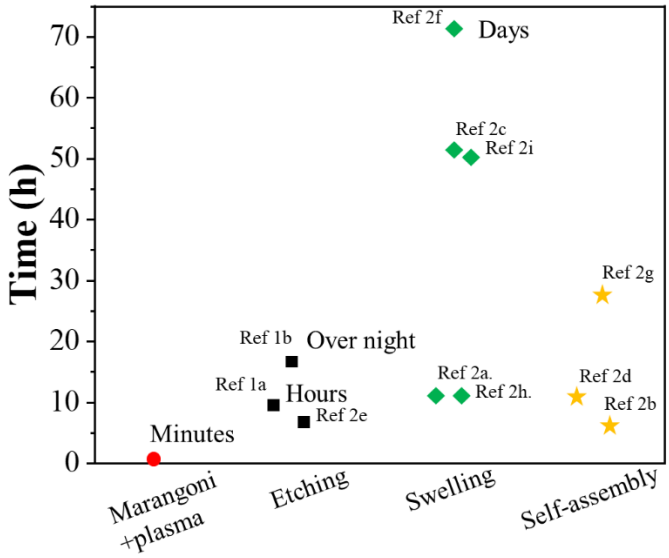

Figure S12. Comparison of our "Marangoni self-assembly" & "plasma etching" method and other assembly methods for PC in terms of assembly time [6-16].

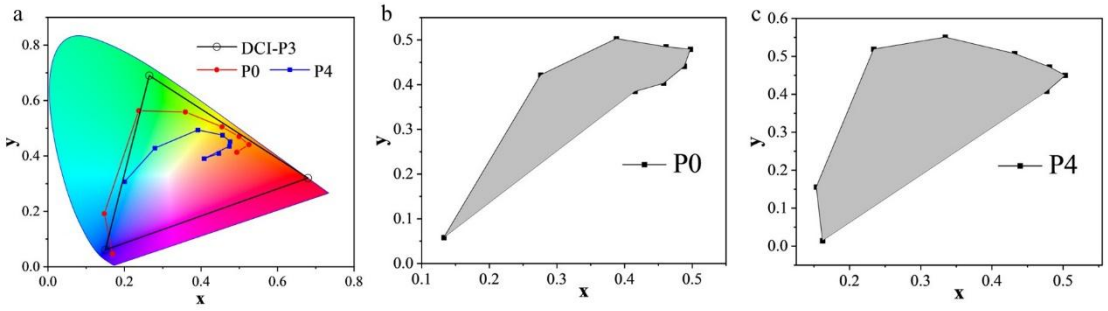

Figure S13. a) Comparison of color gamuts of the P0, P4 devices, and DCI-P3 in the CIE chromaticity diagram. Diagrams of the calculated areas for the b) P0 and c) P4 samples.

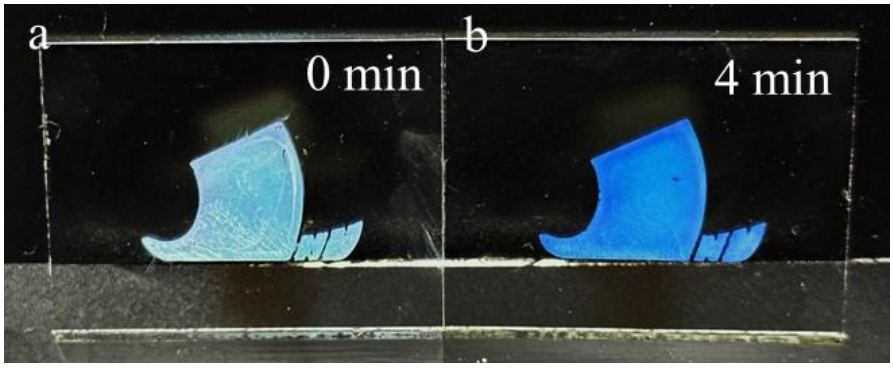

Figure S14. Digital photographs of the PCC film a) without and b) with 4-minute plasma treatment. The treatment (with a large DIP) induces a blue shift with an increased saturation, which facilitates enlarging sensing range of the PCC film.

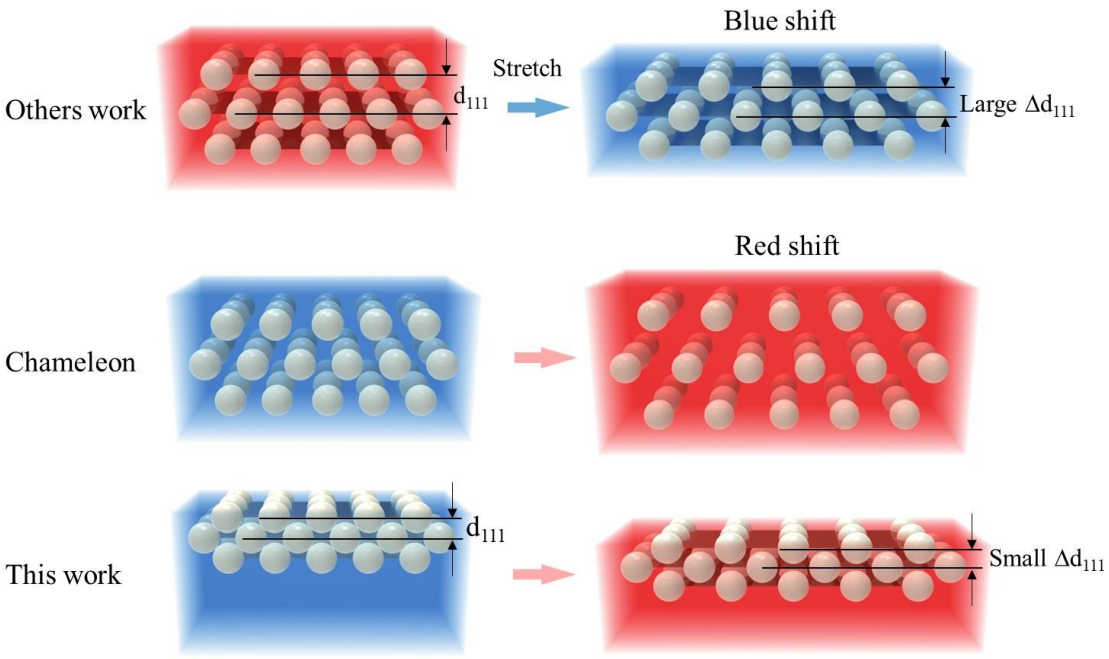

Figure S15. Comparison of the sensing mechanisms for other blue-shift PC sensors, red-shift panther chameleon[17] or *Phelsuma* lizard[18], and the red-shift PE-skin.

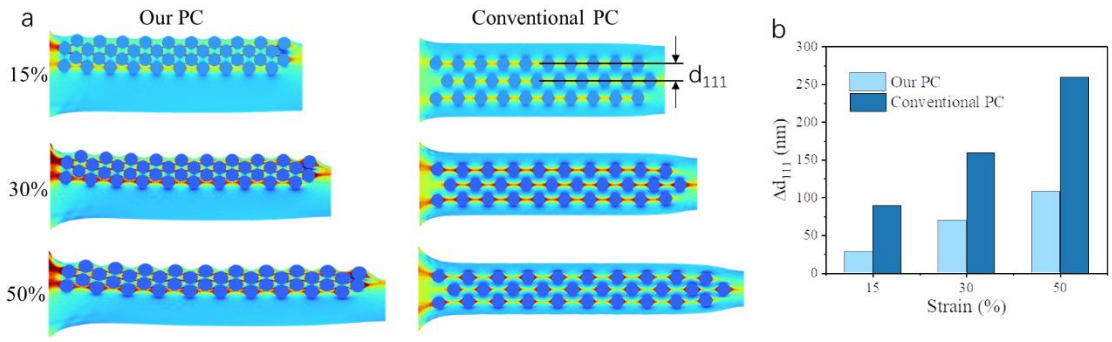

Figure S16. a) Mechanical simulations of our PC and conventional PC under different strains. b) Spacing change (Δd_{111}) of the two types of PCs.

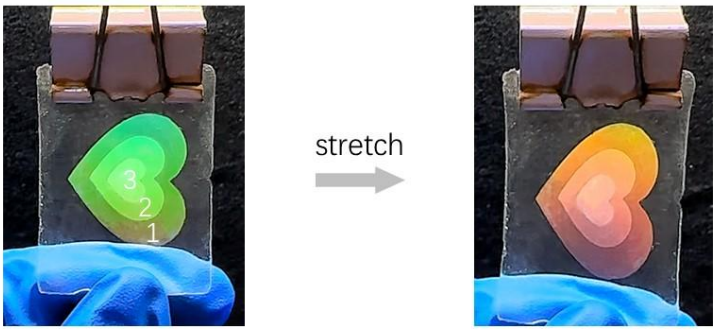

Figure R17. Photograph of the trilayered NP arrays in the PDMS surface before and after stretching. The white numbers denote the layers of the NP array. Structure colors are displayed on the one layer, two layers, and three layers of the NP array. The structural color from a monolayer NP array can only come from the 2D Bragg diffraction.

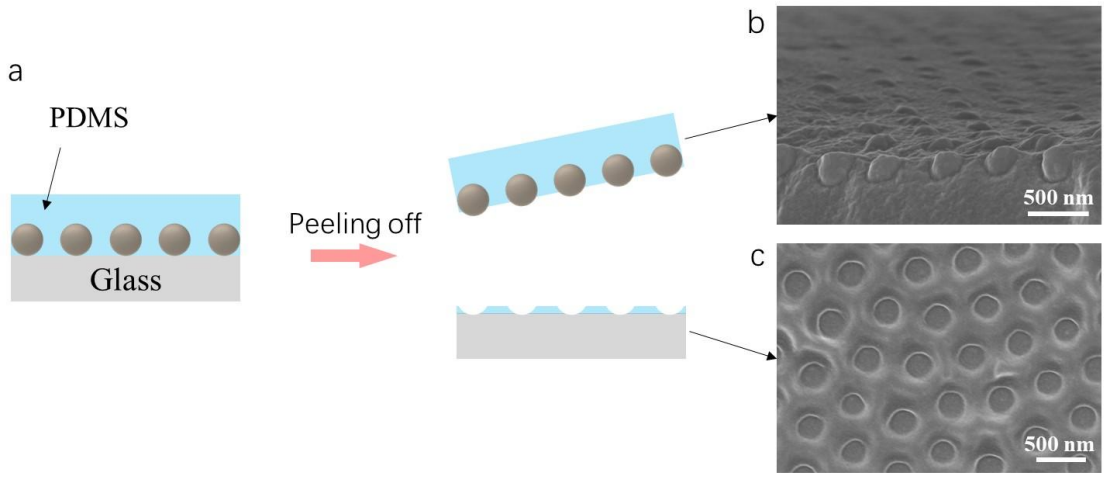

Figure S18. a) Schematic of the PS NP array embedded into the PDMS surface after the transferring process. SEM images of b) the transferred NPs in the PDMS surface and c) the residual PDMS pattern on the donor glass.

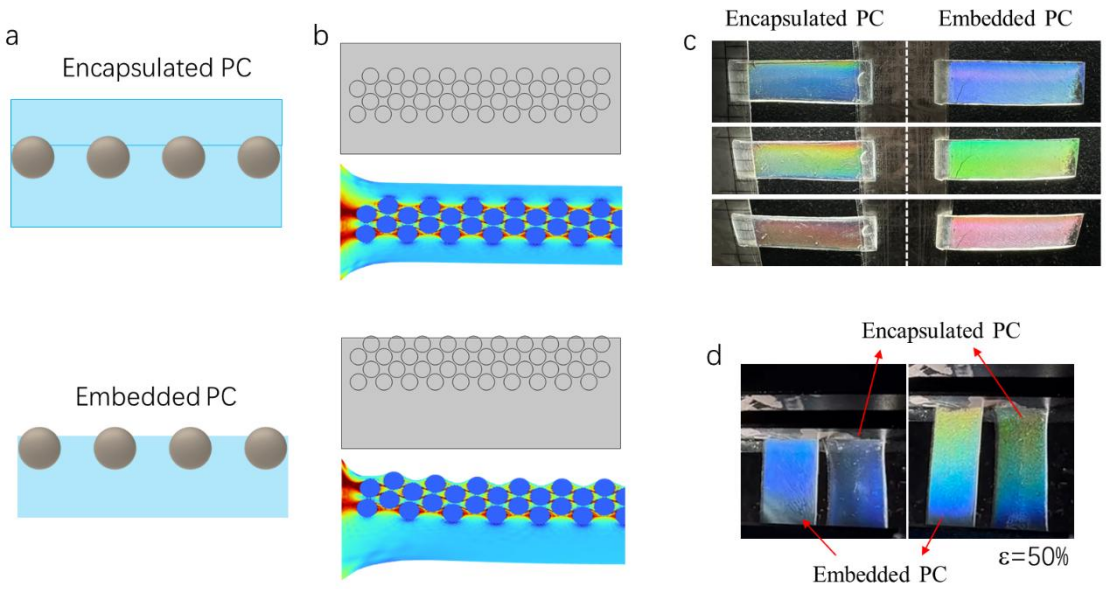

Figure S19. a) Schematics of the encapsulated and embedded PCs in PDMS. b) Mechanical simulation of the encapsulated and embedded at 50% strain, showing a flat surface and a submicron-structural surface at a stretched state. Color comparison of the two PCs under different c) angles and d) stains, demonstrating that the embedded PC with submicron surface structure has more vivid colors than the encapsulated PC.

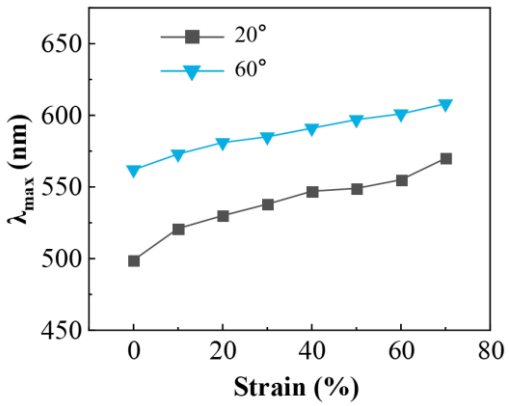

Figure S20. Peak wavelength shifts versus tensile strains of the PC devices with light incident angles of 20° and 60°.

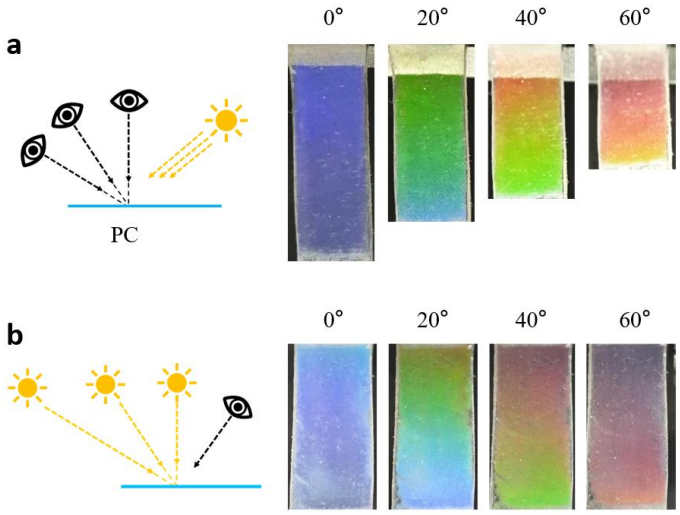

Figure S21. Photographs of diffractions of our PC at (a) different viewing angle and a fixed incident angle of 45° and (b) fixed viewing angle and varied incident angle.

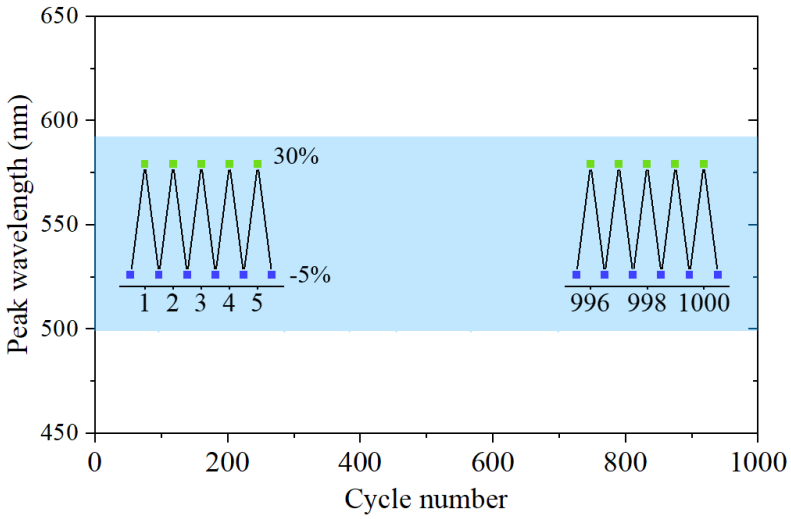

Figure S22. Color switching of the PE-skin under a 1000-time cyclic test, the strain varies between -5% and 30%.

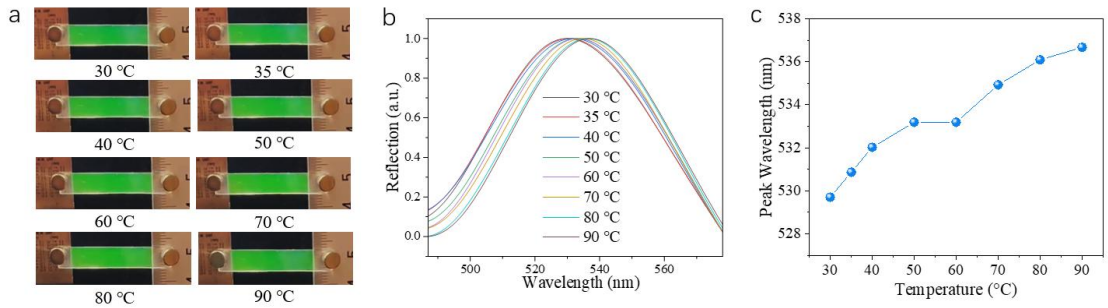

Figure S23. a) Photographs of the PC layer under different temperatures, showing a trivial change on structural colors. b) Reflective spectra and c) peak wavelengths of the PC layer at elevated temperatures. As indicated by these images, no noticeable change in the structural colors can be observed by the naked eye within this temperature range. The spectra reveal that higher temperatures induce a red shift, attributed to the thermal expansion of the PDMS matrix. Specifically, the reflective peaks show a red shift of 6.97 nm for a temperature increase (ΔT) of 60 °C, corresponding to an average temperature sensitivity (defined as $\Delta\lambda/\Delta T$) of 0.116 nm/°C. This low temperature sensitivity leads to minimal changes in color under temperature variations, such as those associated with human skin or natural environments. For instance, human skin typically exhibits a surface temperature between 33 and 37 °C, rising to a maximum of 42 °C during high fever. In this case, the temperature increase induces a wavelength shift of less than 2.3 nm. Such small shifts in wavelength (2–3 nm) are imperceptible to the naked eye.

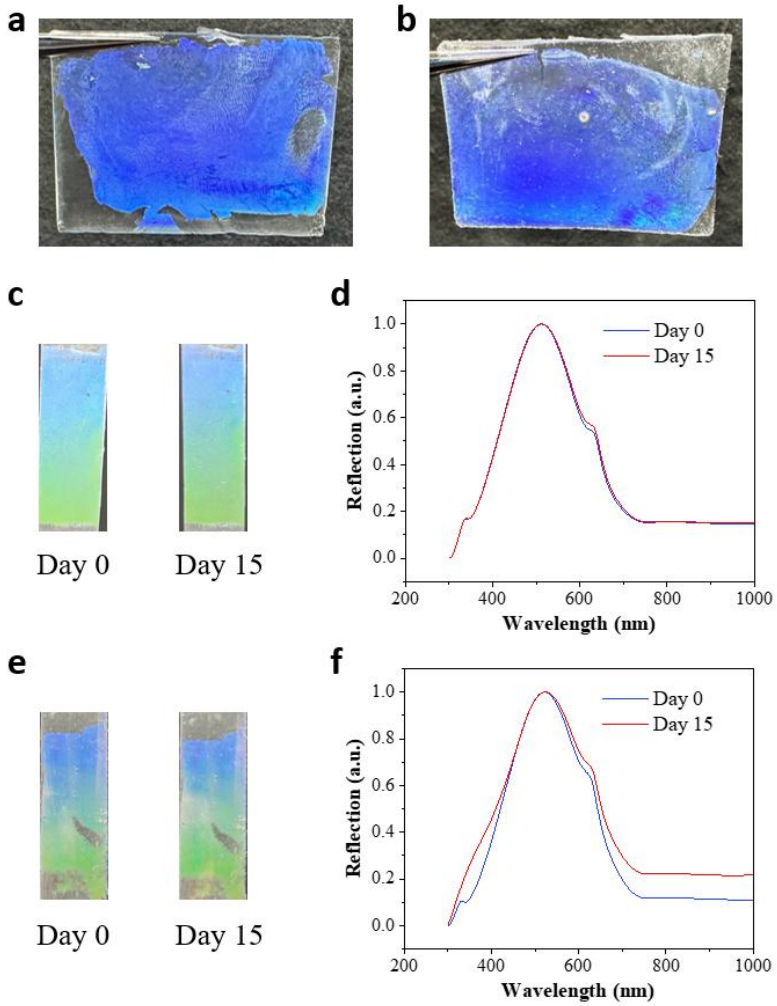

Figure S24. Comparison of a) the fresh PC film and b) the PC film prepared six months ago. c) Photographs and d) spectra of the PC film before and after long-term storage in peanut oil for 15 days. e) Photographs and f) spectra of the PC film before and after long-term storage in high-humidity atmosphere (85% relative humidity at room temperature) for 15 days. No obvious color fading or shift is found in these PC films after storing at different conditions.

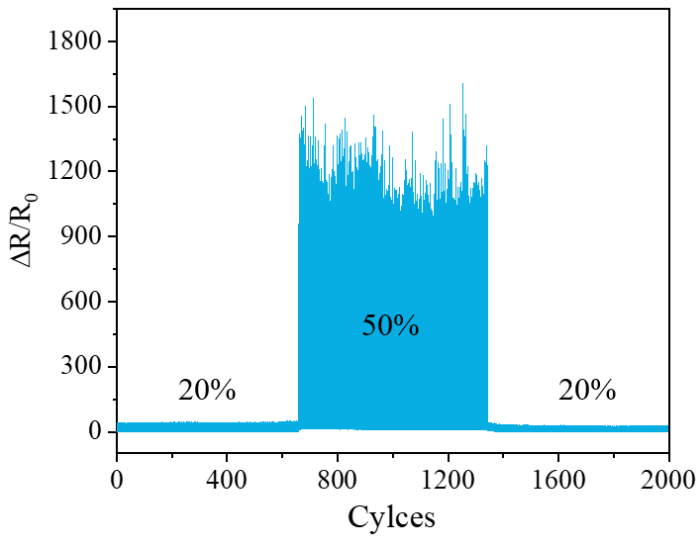

Figure S25. Cyclic response of the MXene/AgNW- PDMS at 20% & 50% strain.

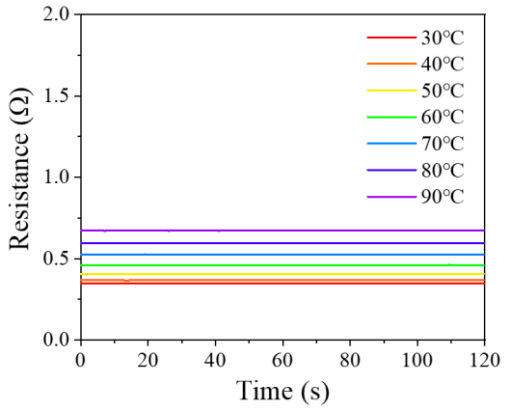

Figure S26. Resistance curves of the resistive MXene/AgNW strain sensors under different temperatures. The resistance of the electronic sensor increases from 0.35 Ω to 0.67 Ω as the environmental temperature rises from 30 to 90 °C. The relative resistance change ($\Delta R/R_0$) is approximately 0.91, which is significantly lower than GF of 228.1 at 10% strain and 2600 at 50% strain.

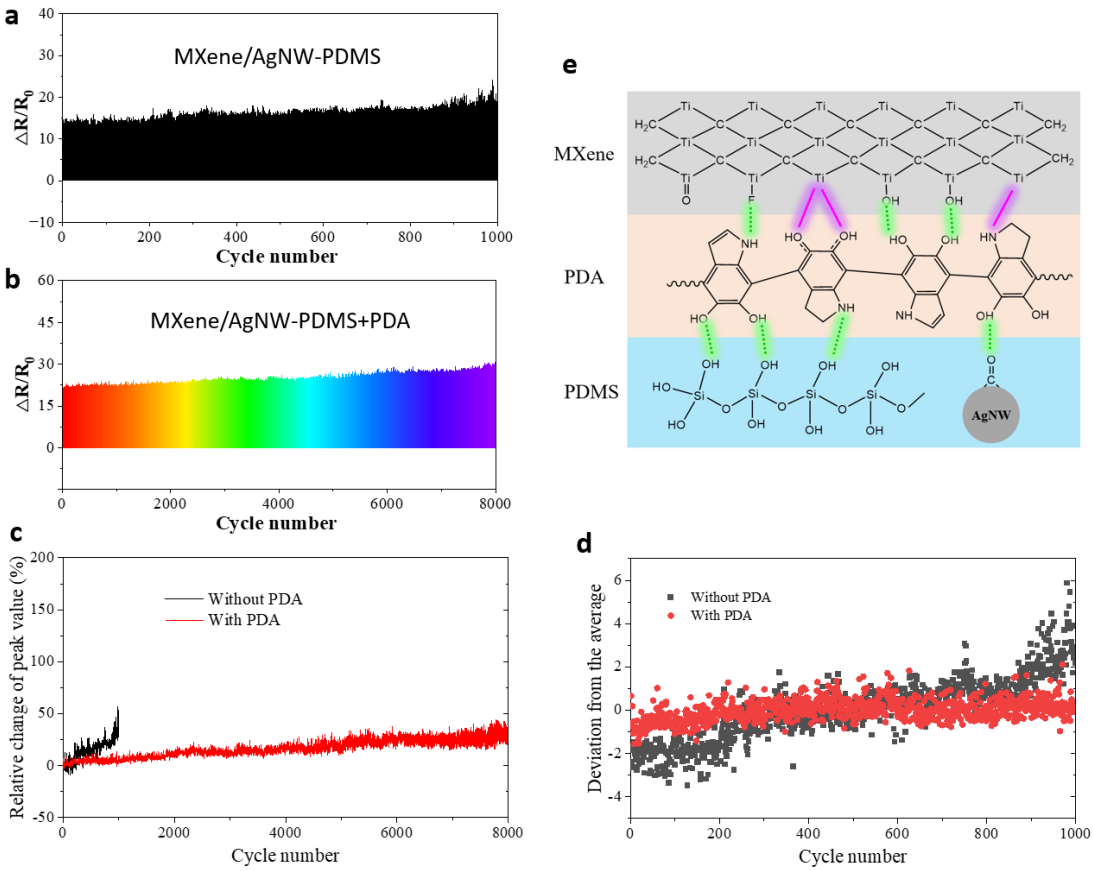

Figure S27. Cyclic test of the MXene/AgNW-PDMS layer a) without and b) with PDA modification. c) Relative change of the peak values under stretching-releasing tests, tensile strain: 10%. d) Deviation from the average of the peak values. e) Schematic of the chemical interaction between PDA and other layers (MXene, oxidized PDMS, and AgNW).

As indicated in (a), the electrical stability under cyclic stretch-releasing is unsatisfactory because of the weak interaction between MXene and the AgNW-PDMS. To improve stability, the AgNW-PDMS surface was first modified by PDA and then coated with MXene. The PDA interlayer has amine and catechol groups to form coordination and hydrogen bonds with the MXene surface. The dopamine can also form hydrogen bonds with the hydroxylated PDMS and carbonyl groups on the surface of AgNWs. These chemical bonds enhance the interface adhesion and improve mechanoelectrical stability. Without PDA modification, the electrical signals have more spikes and peak drift. The relative change of the peak resistance ($(R_{peak}-R_{peak0})/R_{peak0}$) increases by > 50% for the unmodified sensor, whereas the relative change of the PDA-modified sensor is about 10% at the 1000th cycle and only increases to <30% after an 8000-cycle test. Figure (d) shows the difference in the deviation degree from

the average for the two sensors. The standard deviations from the average of the peak values are 1.98 and 0.49 for the modified and unmodified sensors. In short, the mechanoelectrical stability of the MXene/AgNW-PDMS sensor has been effectively improved by PDA modification.

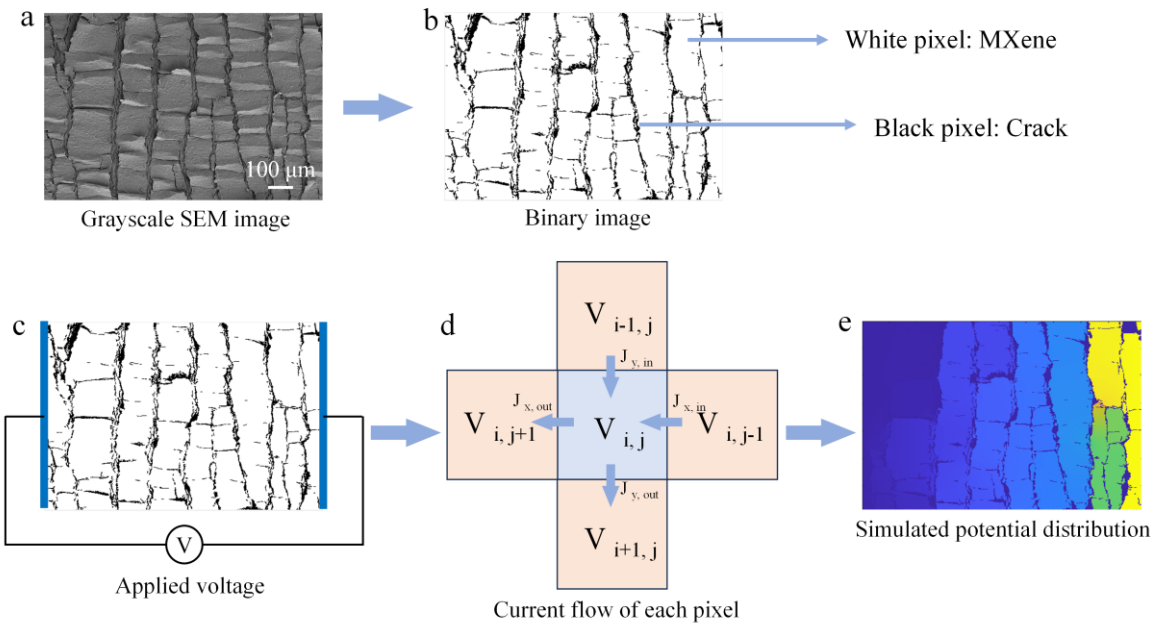

Figure S28. a) Grayscale SEM image of a stretched MXene/AgNW layer with microcracks. b) Converted binary SEM image. c) Applied potential difference (1 V) as the matrix boundary condition. d) The inter-pixel current continuity. e) Simulated voltage distribution based on a numerical method, developed by Wagner‘s group.[19]

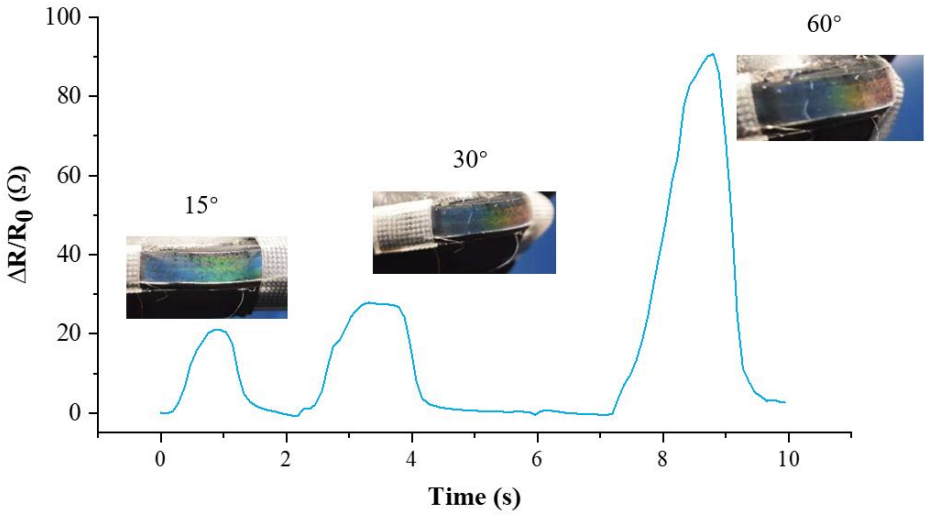

Figure S29. Detection of finger joint movement with the PE-skin. The relative resistance and optical variation of the PE-skin under different bending angles.

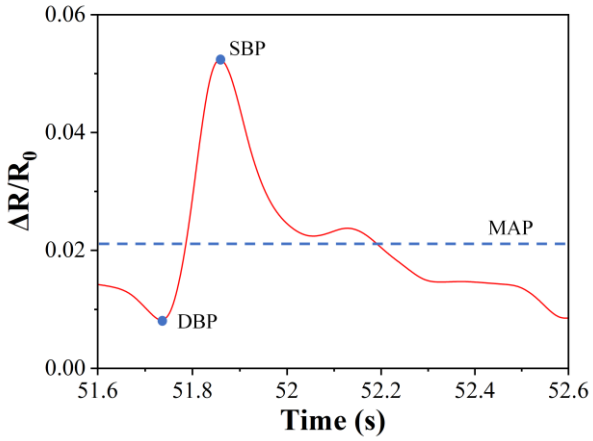

Figure S30. The waveform of one pulse cycle detected by the PE-skin.

The waveform characteristics of pulses reflect cardiovascular diseases. The graph shows the typical pulse waveform from a 22-year-old male, which is to assess vascular health. *Pd* is the diastolic blood pressure (DBP), *Ps* is the systolic blood pressure (SBP), and *Pm* is the mean arterial pressure (MAP), which refers to the average arterial blood pressure throughout the heart cycle. MAP can be calculated by the following formula:

$$Pm = Pd + 1/3 * (Ps - Pd) \quad (1)$$

The *K* value indicates the relationship between the degree of vascular aging and peripheral vascular resistance, and the *K* value is proportional to peripheral vascular resistance. It is defined as:

$$K = \frac{Pm - Pd}{Ps - Pd} \quad (2)$$

Blood viscosity (V) is a measurement method of blood flow resistance, which is closely related to the K value. A rise of blood viscosity usually reflects cardiovascular disease, such as coronary heart disease and heart infarction.

$$V = 11.43 * K \quad (3)$$

Using the single pulse waveform. The values of K and V are calculated to be around 0.33 and 3.81, respectively. As the blood viscosity of a normal young man is in the range of 3~ 4.5, the above results reflect the healthy state of the man's blood vessels.

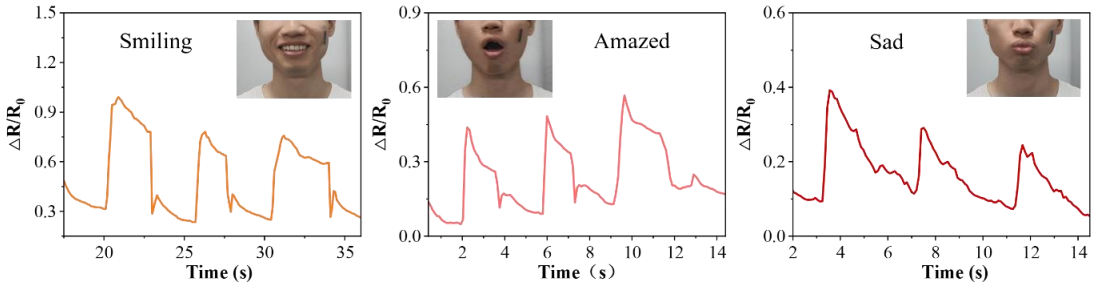

Figure S31. Electrical responses of the PE-skin to various human facial expressions, including a) smiling, b) amazed and c) sad.

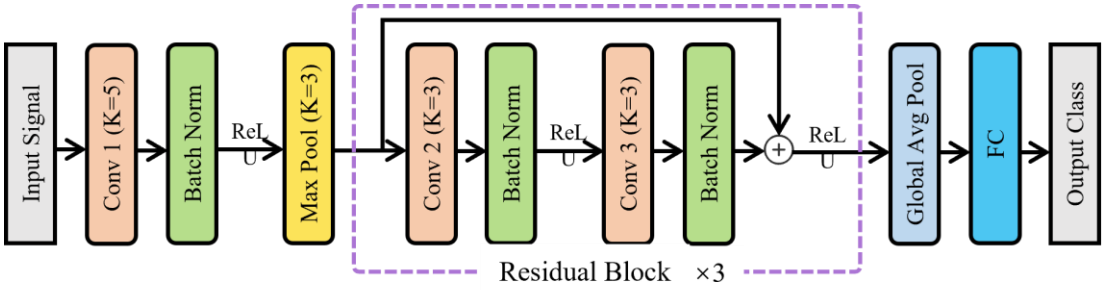

Figure S32. Structure of 1D-ResConv for classification of the resistance signals.

Table S1. Comparison of the PE-skin with reported dual-function sensors in materials, structure, fabrication, and performance

Materials & Structure	**PC fabrication**	**MC behavior**	**Patterning**	**D_{IP}**	**Optical signal**	**Electrical signal**
Hydrogel & Anti-opal[20]	HF etching	Blue shift	No	27 nm	0%→150% Δλ=146 nm 0.97 nm %$^{-1}$	0%→400 % GF < 1
Hydrogel & Anti-opal[7]	HF etching	Blue shift	Yes	30 nm	0%→60% Δλ=214 nm 3.56 nm %$^{-1}$	0%→100 % GF=2.4
Ionogel & PS@SiO_2[8]	Swelling	Blue shift	Yes	19 nm	0%→80% Δλ=154 nm 1.89 nm %$^{-1}$	0%→80% GF=2.31
Hydrogel & Fe_3O_4 NP/ CNT-MXene[9]	Electrostatic, magnetic, steric forces	Blue shift	Yes	530 nm	0%→230% Δλ =250 nm 1.08 nm %$^{-1}$	0%→300 % GF=191.8
Ionogel & CNC LC[10]	Swelling	Blue shift	No	65→195 nm	0%→450% Δλ=179 nm 0.40 nm %$^{-1}$	0%→1000 % GF=3.51
PEGPEA-SiO_2 NP & rGO-PDMS[11]	Solvation layer	Blue shift	No	58 nm	0%→68.2% Δλ=121 nm 1.77 nm %$^{-1}$	0%→30% GF=4.78
Hydrogel & Anti-opal[12]	HF etching	Blue shift	Yes	84 nm	0%→90% ≈200 nm 2.22 nm %$^{-1}$	0%→90% GF=1.67
PDMS& PS/Graphene[13]	Swelling	Blue shift	No	28 nm	0%→30% Δλ=60 nm 2 nm %$^{-1}$	0%-30% GF<2
Ionogel & Fiber of SiO_2 & PEGPEA[14]	Solvation layer	Blue shift	No	23 nm	0%→80% Δλ=121 nm 1.51 nm %$^{-1}$	0%→100 % GF=1.9
Ionogel & Si NPs[15]	Solvation layer	Blue shift	Yes	24 nm	0%→80% Δλ=130 nm 1.6 nm %$^{-1}$	0%→400 % GF=2.3
Ionogel & CNC[16]	Swelling	Blue shift	No	300→443 nm	0%→100% Δλ=201 nm 2.01 nm %$^{-1}$	0%→100 % GF=0.97
This work: A-PDMS & PS NPs	Plasma etching	**Red shift**	Yes	0-280 nm (Tunable)	-15%→70% Δλ=219 nm 2.57 nm %$^{-1}$	0%→50% GF=2600

Table S2. Colloidal nanoparticles-based stretchable photonic crystal for detection of tensile strain (i.e., strain sensors) and compressive strain (i.e., pressure sensors)

Sensing Parameter	MC behavior	Optical signal	Mechanism	Ref
Tensile strain	Blue shift	Δλ=30nm	Order degree of NPs	[21]
	Blue shift	660→550nm	Interplane distance ↓	[22]
	Blue shift	604→558nm	Interplane distance ↓	[23]
	Blue shift	643→465nm	Interplane distance ↓	[24]
	Blue shift	Δλ=276nm	Interplane distance ↓	[25]
	Blue shift	604→550nm	Interplane distance ↓	[26]
	Blue shift	590→394nm	Interplane distance ↓	[27]
	Blue shift	604→500nm	Interplane distance ↓	[28]
	Blue shift	635→434nm	Interplane distance ↓	[29]
	Blue shift	-	Interplane distance ↓	[30]
	Blue shift	680→430nm	Interplane distance ↓	[31]
	Blue shift	640→540nm	Interplane distance ↓	[32]
	Blue shift	630→425nm	Interplane distance ↓	[33]
	Blue shift	yellow to blue	Interplane distance ↓	[34]
	Blue shift	525→487nm	Interplane distance ↓	[35]
	Blue shift	1101→1046nm	Interplane distance ↓	[36]
	Blue shift	618→490nm	Interplane distance ↓	[37]
	Blue shift	653→507nm	Interplane distance ↓	[20]
	Blue shift	647→433nm	Interplane distance ↓	[7]
	Blue shift	632→478nm	Interplane distance ↓	[8]
	Blue shift	680→430nm	Interplane distance ↓	[9]
	Blue shift	735→556nm	Interplane distance ↓	[10]
	Blue shift	618→497nm	Interplane distance ↓	[11]
	Blue shift	635→430nm	Interplane distance ↓	[12]
	Blue shift	580→520nm	Interplane distance ↓	[13]
	Blue shift	608→487nm	Interplane distance ↓	[14]
	Blue shift	610→480nm	Interplane distance ↓	[15]
	Blue shift	610→420nm	Interplane distance ↓	[38]
	Red shift	510→780nm	2D diffraction	
	Red shift	green to yellow/ orange	In-plane distance ↑	[39] **(Chameleon)**
	Red shift	661→442nm	In-plane distance ↑	**This work**
Compressive strain	Blue shift	730→700nm	Order degree of NP ↓	[40]

	Blue shift	655→665nm	Order degree of NP ↓	[21]
	Blue shift	680→620nm	Interplane distance ↓	[41]
	Blue shift	635→434nm	Interplane distance ↓	[29]
	Blue shift	790→488nm	Interplane distance ↓	[42]
	Blue shift	510→410nm	Interplane distance ↓	[35]
	Blue shift	619→591nm	Interplane distance ↓	[37]
	Blue & Red shift	460→630nm	Inter-cluster distance↓↑	[43]

Table S3. Hyperparameters of 1D-ResCov

Layer		Channels	Kernal Size	Stride	Padding
Conv 1 (K=5)		32	5	2	2
Max Pool (K=3)		32	3	2	1
Residual Block 1	Conv 2 (K=3)	32	3	1	1
	Conv 3 (K=3)	32	3	1	1
Residual Block 2	Conv 2 (K=3)	64	3	2	1
	Conv 3 (K=3)	64	3	1	1
Residual Block 3	Conv 2 (K=3)	128	3	2	1
	Conv 3 (K=3)	128	3	1	1

References

1. Kang, D. et al. Ultrasensitive mechanical crack-based sensor inspired by the spider sensory system. **516**, 222-226 (2014).
2. Choi, Y.W. et al. Ultra-sensitive pressure sensor based on guided straight mechanical cracks. **7**, 40116 (2017).
3. Lee, P. et al. Highly stretchable and highly conductive metal electrode by very long metal nanowire percolation network. **24**, 3326-3332 (2012).
4. Amjadi, M. et al. Highly stretchable and sensitive strain sensor based on silver nanowire–elastomer nanocomposite. **8**, 5154-5163 (2014).
5. Ba, O.M. et al. Surface composition XPS analysis of a plasma treated polystyrene: Evolution over long storage periods. *Colloids and Surfaces B: Biointerfaces* **145**, 1-7 (2016).
6. Zhang, H. et al. Stretchable and conductive composite structural color hydrogel films as bionic electronic skins. **8**, 2102156 (2021).
7. Wang, Y. et al. Bio-Inspired Stretchable, Adhesive, and Conductive Structural Color Film for Visually Flexible Electronics. *Advanced Functional Materials* **30**, 2000151 (2020).
8. Sun, Y. et al. Biomimetic Chromotropic Photonic-Ionic Skin with Robust Resilience, Adhesion, and Stability. *Advanced Functional Materials* **32** (2022).
9. Zhang, H. et al. Mechanochromic Optical/Electrical Skin for Ultrasensitive Dual-Signal Sensing. *ACS Nano* **17**, 5921-5934 (2023).
10. Li, X. et al. Polymerizable deep eutectic solvent-based skin-like elastomers with dynamic schemochrome and self-healing ability. *Small* **18**, 2201012 (2022).
11. Xu, H. et al. Dual-Mode Wearable Strain Sensor Based on Graphene/Colloidal Crystal Films for Simultaneously Detection of Subtle and Large Human Motions. *Advanced Materials Technologies* **5**, 1901056 (2020).
12. Liu, H. et al. Fast Self-Assembly of Photonic Crystal Hydrogel for Wearable Strain and Temperature Sensor. *Small Methods* **6**, e2200461 (2022).
13. Snapp, P. et al. Colloidal Photonic Crystal Strain Sensor Integrated with Deformable Graphene Phototransducer. *Advanced Functional Materials* **29** (2019).
14. Zhao, R. et al. Dual-Mode Fiber Strain Sensor Based on Mechanochromic Photonic Crystal and Transparent Conductive Elastomer for Human Motion Detection. *ACS Appl Mater Interfaces* **15**, 16063-16071 (2023).
15. Peng, L., Hou, L. & Wu, P. Synergetic Lithium and Hydrogen Bonds Endow Liquid-Free Photonic Ionic Elastomer with Mechanical Robustness and Electrical/Optical Dual-Output. *Adv Mater* **35**, e2211342 (2023).
16. Li, X. et al. Mechanochromic and Conductive Chiral Nematic Nanostructured Film for Bioinspired Ionic Skins. *ACS Nano* **17**, 12829-12841 (2023).
17. Teyssier, J. et al. Photonic crystals cause active colour change in chameleons. *Nature Communications* **6**, 6368 (2015).
18. Saenko, S.V. et al. Precise colocalization of interacting structural and pigmentary elements generates extensive color pattern variation in Phelsumalizards. *BMC Biology* **11**, 105 (2013).

19. Cao, W., Görrn, P. & Wagner, S. Modeling the electrical resistance of gold film conductors on uniaxially stretched elastomeric substrates. *Applied Physics Letters* **98** (2011).
20. Zhang, H. et al. Stretchable and Conductive Composite Structural Color Hydrogel Films as Bionic Electronic Skins. *Adv Sci (Weinh)* **8**, e2102156 (2021).
21. Hu, F. et al. Gel-based artificial photonic skin to sense a gentle touch by reflection. *ACS applied materials & interfaces* **11**, 15195-15200 (2019).
22. Tan, H. et al. Metallosupramolecular Photonic Elastomers with Self-Healing Capability and Angle-Independent Color. *Adv Mater* **31**, e1805496 (2019).
23. Zhao, K. et al. Interactively mechanochromic electronic textile sensor with rapid and durable electrical/optical response for visualized stretchable electronics. *Chemical Engineering Journal* **426**, 130870 (2021).
24. Wang, Y. et al. Cephalopod-Inspired Chromotropic Ionic Skin with Rapid Visual Sensing Capabilities to Multiple Stimuli. *ACS Nano* **15**, 3509-3521 (2021).
25. Xie, Y. et al. Bistable and reconfigurable photonic crystals—electroactive shape memory polymer nanocomposite for ink-free rewritable paper. *Advanced Functional Materials* **28**, 1802430 (2018).
26. Wang, Y. et al. Bioinspired structural color patch with anisotropic surface adhesion. *Science Advances* **6**, eaax8258 (2020).
27. Lin, R. et al. Bio-Inspired Wrinkled Photonic Elastomer with Superior Controllable and Mechanically Stable Structure for Multi - Mode Color Display. *Advanced Functional Materials* **32**, 2207691 (2022).
28. Lyu, Q. et al. Bioinspired photonic ionogels as interactively visual ionic skin with optical and electrical synergy. *Small* **17**, 2103271 (2021).
29. Bai, L. et al. Bio-inspired visual multi-sensing interactive ionic skin with asymmetrical adhesive, antibacterial and self-powered functions. *Chemical Engineering Journal* **438**, 135596 (2022).
30. Fu, F. et al. Bio-inspired self-healing structural color hydrogel. *Proceedings of the National Academy of Sciences* **114**, 5900-5905 (2017).
31. Zhang, H. et al. Bioinspired Chromotropic Ionic Skin with In - Plane Strain/Temperature/Pressure Multimodal Sensing and Ultrahigh Stimuli Discriminability. *Advanced Functional Materials* **32**, 2208362 (2022).
32. Niu, W. et al. Photonic Vitrimer Elastomer with Self - Healing, High Toughness, Mechanochromism, and Excellent Durability based on Dynamic Covalent Bond. *Advanced Functional Materials* **31** (2021).
33. Hu, Y. et al. Chameleon-Inspired Brilliant and Sensitive Mechano-Chromic Photonic Skins for Self-Reporting the Strains of Earthworms. *ACS Appl Mater Interfaces* **14**, 11672-11680 (2022).
34. Park, J. et al. A hierarchical nanoparticle - in - micropore architecture for enhanced mechanosensitivity and stretchability in mechanochromic electronic skins. *Advanced Materials* **31**, 1808148 (2019).
35. Yang, D., Ye, S. & Ge, J. From metastable colloidal crystalline arrays to fast responsive

mechanochromic photonic gels: An organic gel for deformation-based display panels. *Advanced Functional Materials* **24**, 3197-3205 (2014).

36. Li, J. et al. Reversibly strain-tunable elastomeric photonic crystals. *Chemical physics letters* **390**, 285-289 (2004).
37. Lee, G.H. et al. Chameleon-Inspired Mechanochromic Photonic Films Composed of Non-Close-Packed Colloidal Arrays. *ACS Nano* **11**, 11350-11357 (2017).
38. Chen, J. et al. Highly Stretchable Photonic Crystal Hydrogels for a Sensitive Mechanochromic Sensor and Direct Ink Writing. *Chemistry of Materials* **31**, 8918-8926 (2019).
39. Teyssier, J. et al. Photonic crystals cause active colour change in chameleons. *Nat Commun* **6**, 6368 (2015).
40. Wang, X. et al. Chameleon-inspired flexible photonic crystal lens-shaped dynamic pressure sensor based on structural color shift. *Cell Reports Physical Science* **4** (2023).
41. Arsenault, A.C. et al. From colour fingerprinting to the control of photoluminescence in elastic photonic crystals. *Nature Materials* **5**, 179-184 (2006).
42. Hu, Y. et al. Extremely sensitive mechanochromic photonic crystals with broad tuning range of photonic bandgap and fast responsive speed for high-resolution multicolor display applications. *Chemical Engineering Journal* **429** (2022).
43. Wang, X.Q. et al. Hydrogels: Robust Mechanochromic Elastic One-Dimensional Photonic Hydrogels for Touch Sensing and Flexible Displays (Advanced Optical Materials 7/2014). **2**, 651-651 (2014).